# High-Performance InP-Based Bias-Tunable Near-Infrared/Extended-Short Wave Infrared Dual-Band Photodetectors

Zongti Wang, Jian Huang, Liqi Zhu, Zhiqi Zhou, Xuyi Zhao, Antian Du, Wenfu Yu, Ruotao Liu, Qian Gong, and Baile Chen, *Senior Member, IEEE*

***Abstract*—In this paper, a vertical stacked near-infrared (NIR) and extended short wavelength infrared (eSWIR) dual-band detector based on InGaAs and $In_{0.53}Ga_{0.47}As/GaAs_{0.5}Sb_{0.5}$ type-II superlattice (T2SL) is presented. A barrier layer of $AlAs_{0.56}Sb_{0.44}$ allows the independent working of the two sub-detectors. The InGaAs NIR sub-detector operates under positive bias, while the eSWIR band detector operates under reverse bias. The NIR sub-detector shows a dark current density of $7.35 \times 10^{-5}$ A/cm$^2$ under the bias of 0.1 V, the responsivity of 0.88 A/W, and a specific detectivity of $4.69 \times 10^{11}$ cm· Hz$^{1/2}$/W at 1510 nm. Meanwhile, the dark current density of eSWIR sub-detector is $8.68 \times 10^{-4}$ A/cm$^2$ under −0.4 V with the corresponding responsivity of 0.21 A/W, and a specific detectivity of $1.85 \times 10^{10}$ cm·Hz$^{1/2}$/W at 2 $\mu$m. Furthermore, a single-pixel imaging system is built to demonstrate the capability of dual-band detectors in information capturing and target recognition.**

***Index Terms*—Dual-band, $In_{0.53}Ga_{0.47}As$ PIN, $In_{0.53}Ga_{0.47}As/GaAs_{0.5}Sb_{0.5}$ T2SL, NIR /eSWIR photodetector, single pixel imaging.**

## I. Introduction

RECENTLY, high-performance multiple band infrared photodetectors have attracted intense interest. The spectral information of distinct bands can improve the identification of targets in complex environments. Thus, multi-band detectors have many applications in biomedical imaging, spectral sensing, environmental monitoring, and other fields [1], [2]. Conventional multi-band detectors are based on complex imaging techniques that require the introduction of beam splitters, filters, and other components in the optical path, which increases the complexity of multi-band detection. In contrast, a single imaging device with dual-band detection capability can eliminate the need for multi-element optical path alignment, greatly reducing the complexity of multi-band imaging systems [3]. Visible light (VL) has a limited propagation distance and visibility in the scattering medium due to Rayleigh scattering. On the other hand, short-wave infrared (SWIR) has a much longer penetration depth in environments such as fog and smoke [4]. This property allows higher visibility of SWIR detectors in severe weather environments and has great potential for autonomous driving and drone inspection [5]. Type-II superlattice (T2SL) has a wide range of applications in infrared detection because of its ability to modulate bandwidth by changing components and thickness while maintaining lattice-matched [6] or strain-balanced conditions [7]. Recently, dual-band detectors operating in SWIR, mid-wavelength infrared (MWIR), and long-wavelength infrared (LWIR) regimes based on InAs/GaSb or InAs/InAsSb type-II superlattices (T2SL) have been reported [8]–[10]. Photodetectors operating in near Infrared (NIR) and eSWIR were first demonstrated based on $In_{0.53}Ga_{0.47}As/GaAs_{0.5}Sb_{0.5}$ T2SL [11], [12] and then later on GeSn /GeSi [13], and In-rich $In_xGa_{1-x}As$ /InP [14]. $In_{0.53}Ga_{0.47}As/GaAs_{0.5}Sb_{0.5}$ T2SL based photodetector enjoys the advantage of lattice matching to InP substrate and thus low dark current as compared to the In-rich $In_xGa_{1-x}As$ photodetector and GeSn photodetector, which is an important candidate for SWIR detection [15]–[24]. The previously reported NIR /eSWIR dual-band detector based on $In_{0.53}Ga_{0.47}As/GaAs_{0.5}Sb_{0.5}$ T2SL by Z. Xie *et al.* has three terminals to avoid the optical crosstalk [11], which increases the complexity of the imaging system and cost of the fabrication process.

In this paper, a vertical stacked NIR /eSWIR dual-band detector based on the $In_{0.53}Ga_{0.47}As/GaAs_{0.5}Sb_{0.5}$ T2SL material system is designed. Instead of introducing an additional metal contact to reduce optical crosstalk, an $AlAs_{0.56}Sb_{0.44}$ barrier layer is incorporated into the structure. The barrier allows tuning the operating band by changing the voltage in a two terminal mesa configuration while maintaining low optical crosstalk [8]–[10]. Moreover, this configuration is compatible with the focal-plane-arrays (FPAs) process by simply inverting the epi-layers. The NIR sub-device covers the spectrum from 850 nm to 1750

Manuscript received 10 March 2022; revised 22 April 2022; accepted 27 April 2022. Date of publication 29 April 2022; date of current version 2 August 2022. This work was supported in part by the National Key Research and Development Program of China under Grant 2019YFB2203400 and in part by the National Natural Science Foundation of China under Grant 61975121. *(Corresponding author: Baile Chen.)*

Zongti Wang, Jian Huang, Liqi Zhu, Zhiqi Zhou, and Baile Chen are with the School of Information Science and Technology, ShanghaiTech University, Shanghai 201210, China, and also with the Shanghai Engineering Research Center of Energy Efficient and Custom AI IC, Shanghai 201210, China (e-mail: wangzt@shanghaitech.edu.cn; huangjian@shanghaitech.edu.cn; zhulq@shanghaitech.edu.cn; zhouzq@shanghaitech.edu.cn; chenbl@shanghaitech.edu.cn).

Xuyi Zhao, Antian Du, Wenfu Yu, Ruotao Liu, and Qian Gong are with the Key Laboratory of Terahertz Solid State Technology, Shanghai Institute of Microsystem and Information Technology, Chinese Academy of Sciences, Shanghai 200050, China (e-mail: xyzhao@mail.sim.ac.cn; 386757265@qq.com; wfyu@mail.sim.ac.cn; liurt@mail.sim.ac.cn; qgong@mail.sim.ac.cn).

Color versions of one or more figures in this article are available at https://doi.org/10.1109/JLT.2022.3171224.

Digital Object Identifier 10.1109/JLT.2022.3171224

nm with a responsivity of 0.88 A/W at 1510 nm under 0.1 V, and the corresponding specific detectivity of $4.69 \times 10^{11}$ cm·$Hz^{1/2}$/W. The eSWIR sub-detector covers the spectrum from 1700 nm to 2400 nm under −0.4 V. The responsivity at 2 $\mu$m is 0.21 A/W with a specific detectivity of $1.85 \times 10^{10}$ cm·$Hz^{1/2}$/W, which is on the same order of magnitude as commercial detectors [25].

## II. Device Structure

The epitaxial structure of the designed dual-band detector is shown in Fig. 1(a). The wafer was grown on InP by solid source molecular beam epitaxy (MBE). The dual-band detector contains a NIR and an eSWIR sub-detector. The epitaxial growth started from the eSWIR sub-detector. The eSWIR sub-detector consists of 500 nm n-type doped InGaAs layer, 100 periods unintentionally doped (UID) $In_{0.53}Ga_{0.47}As/GaAs_{0.5}Sb_{0.5}$ T2SL absorption layer, and 50 periods p-type doped $In_{0.53}Ga_{0.47}As/GaAs_{0.5}Sb_{0.5}$ T2SL. The NIR sub-detector consists of 500 nm p-type doped InGaAs layer, 2000 nm unintentionally doped (UID) InGaAs layer, 20 nm n-type doped InAlAs, and 10 nm n-type doped InGaAs layer. A 200 nm p-type doped $AlAs_{0.56}Sb_{0.44}$ barrier layer is inserted between the NIR and eSWIR sub-detectors. The X-ray diffraction (XRD) $\omega$-2$\theta$ scan of the epitaxial wafer sample is shown in Fig.1(c). It can be observed that there is a slight deviation between the peak of InP substrate and 0th peak of SLs, which indicates a small mismatch between the grown SLs and InP substrate. The period thickness $d$ of the T2SL can be calculated by [11]: $d = \lambda/(2\Delta\theta \cos\theta)$, where $\lambda = 0.15406$ nm is the wavelength of X-ray source, $\Delta\theta$ is the interval between two adjacent satellite peaks, and $\theta$ is the location of the main peak. The calculated period thickness of the T2SL is 9.79 nm which is very close to the designed thickness (10 nm).

The energy band diagram of the detector under 0.1 V and −0.4 V stimulated by commercial software Silvaco TCAD is shown in Fig. 2(a) and (b), respectively. Under 0.1 V, the photo-generated electrons in the T2SL layer are blocked by the $AlAs_{0.56}Sb_{0.44}$ barrier, allowing the detector to work in the NIR band independently, and vice versa under −0.4 V. Due to the incorporation of the barrier layer in the structure, the sub-detectors operating in two bands can work independently without introducing additional intermediate contact electrodes [8], [9].

After the material growth, the wafer was processed into a set of different sizes of mesa-shaped devices with diameters varying from 50 $\mu$m to 500 $\mu$m. Standard photolithography and wet chemical etchant ($H_3PO_4$:$H_2O_2$:$H_2O$ = 1:1:10) were used to define the mesa, and the wet etch stopped at 500 nm thick InGaAs bottom contact layer. Ge/Au/Ni/Au metals were deposited on the top and bottom InGaAs contact layer by e-beam evaporation to form ohmic contacts. Finally, the mesa surfaces were passivated by the SU-8 photoresist [26]–[30].

## III. Results and Discussion

The electrical performance of the detector is measured by a semiconductor parameter analyzer from 160 to 300 K in a cryogenic probe station. The measured dark current-voltage

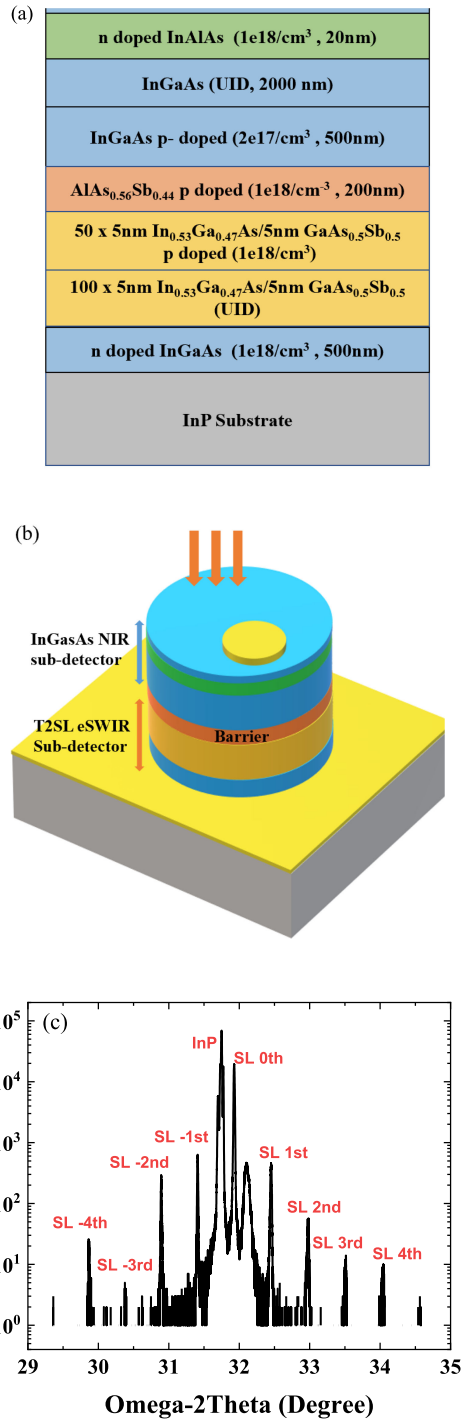


Fig. 1. (a) The schematic diagram of the photodetector structure. (b) The detector structure after fabrication. (c) High resolution X-Ray diffraction pattern of the structure.

curve of a 130 $\mu$m device is shown in Fig. 3. The dark current is $9.76 \times 10^{-9}$ A for NIR sub-detector under 0.1 V at 300 K, which corresponds to a dark current density of $7.35 \times 10^{-5}$ A/cm$^2$. The eSWIR sub-detector proves a dark current density of $8.68 \times 10^{-4}$ A/cm$^2$ at 300 K under a bias of −0.4 V, which is more than an order of magnitude smaller than the previous reported InGaAs/GaAsSb T2SL eSWIR dual-band detector [11]. Fig. 4 displays

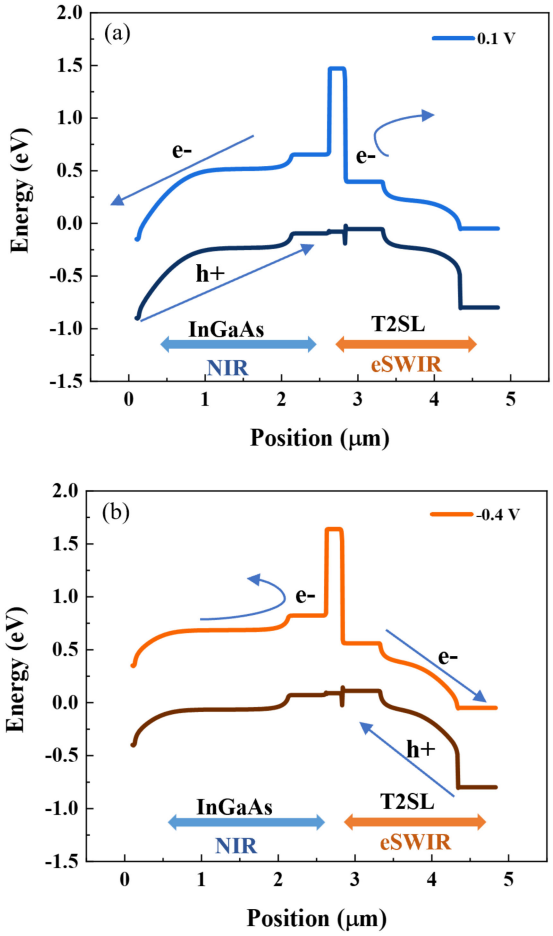


Fig. 2. (a) Simulated energy band diagram of the detector under 0.1 V; (b) Simulated energy band diagram of the detector under −0.4 V, where e- represents electrons, h+ represents holes, and the arrow indicates the direction of carrier motion.

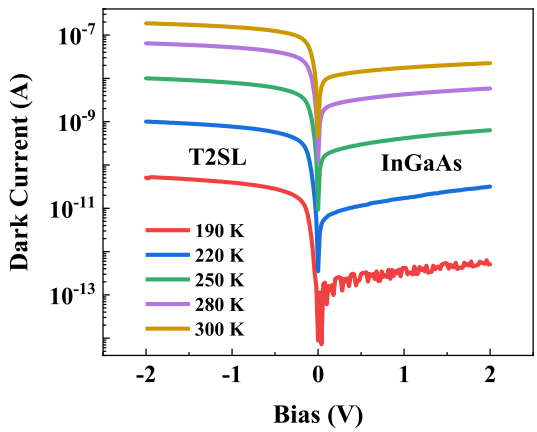


Fig. 3. Dark current-voltage curve for the dual-band photodetector from 190 K to 300 K.

the Arrhenius plot at 0.5 V and −0.5 V in the temperature ranging from 190 K to 300 K. The activation energy $E_{a1}$ is about 0.482 eV, and $E_{a2}$ is about 0.374 eV, which is larger than half of the bandgap energy of InGaAs and T2SL, respectively, indicating that dark current for both sub-detectors are dominated by the diffusion current and generation-recombination (G-R) current.

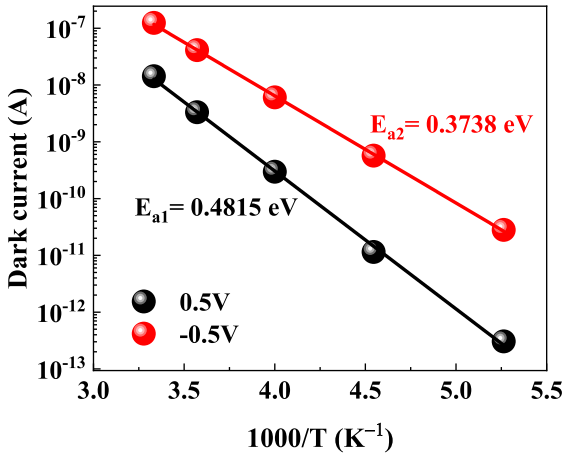


Fig. 4. The Arrhenius plot of the dark current versus temperature under 0.5 V and −0.5 V.

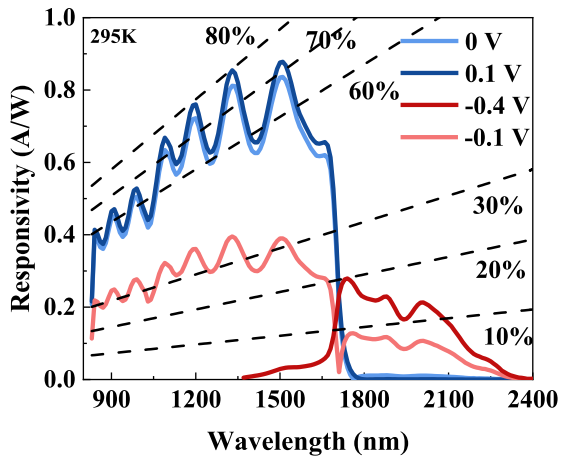


Fig. 5. The dual-band responsivity of the detector from 0.4 V to −0.4 V under room temperature. The NIR sub-detector response saturates at 0.1 V and the eSWIR sub-detector response saturates at −0.4 V, dashed line is quantum efficiency contour indicating the quantum efficiency at the corresponding wavelength.

The optical characteristics is performed in front-side illumination configuration. Monochromatic light is emitted from a halogen lamp passing through a grating spectrometer and is focused on the device. And a 180 Hz chopper is added to the optical path, allowing the optical signal to be amplified by the lock-in amplifier. The responsivity curves under different biases are measured with Thorlab's InGaAs standard detector (part No. PDA10DT-EC) and Si standard detector (part No. FDS1010-CAL) as shown in Fig. 5. The NIR sub-detector reaches a peak responsivity of 0.88 A/W at 1510 nm at 0.1 V. While the bias voltage decreases to a negative value, the response at the NIR band decreases rapidly, and the response at the eSWIR band increases. The device begins to switch to operate in the eSWIR band. The responsivity of eSWIR sub-detector reaches saturation at −0.4 V with a peak responsivity of 0.28 A/W at 1740 nm. The quantum efficiency reaches 72.11% at 1510 nm under 0.1 V, larger than the previously reported work [11]. This can be explained by the improved carrier collection efficiency

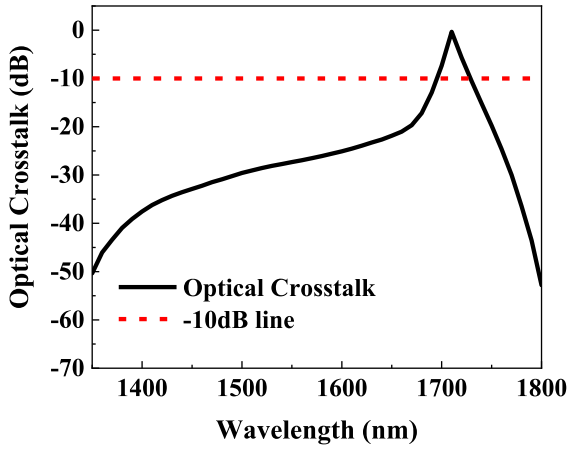


Fig. 6. Calculated optical crosstalk between the two sub-detectors at operating voltage (0.1 V and −0.4 V). The color blocks indicate the operation wavelength band at the corresponding voltage.

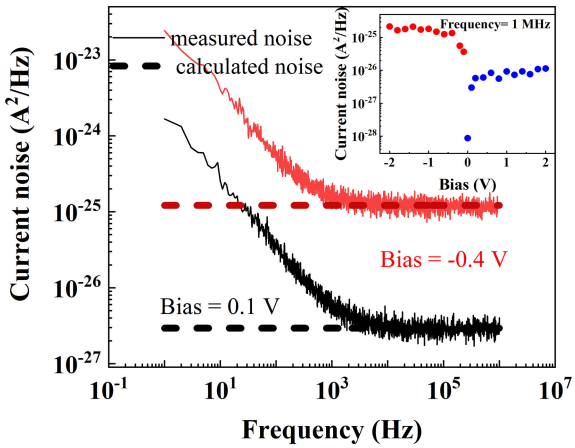


Fig. 7. Current noise power spectral densities as a function of frequency measured under 0.1 V and −0.4 V (solid curves). The noise values calculated by (3) at corresponding biases are also shown (dashed lines). The inset shows the dependences of measured noise on bias extracted at 1 MHz.

with non-absorbing InAlAs n-contact layer. It is noted that the wavy shape of the response curve is caused by the interference between the SU-8 passivation layer and the surface of the device. The interference is constructive or destructive with different wavelengths of monochromatic light.

$$C = -20log_{10}\frac{max\,(QE_{NIR},\ QE_{eSWIR})}{min\,(QE_{NIR},\ QE_{eSWIR})}dB \qquad (1)$$

The optical crosstalk of the two sub-detectors is calculated by (1) which is defined based on the ratio between photocurrent of the two sub-detector, where $QE_{NIR}$ and $QE_{eSWIR}$ are the quantum efficiency of the NIR sub-detector and eSWIR sub-detector, respectively [31]. The calculated result is shown in Fig. 6, the crosstalk peaks at 1710 nm and rapidly decreases to below −10 dB outside 1690 nm and 1730 nm range. The thick InGaAs layer in the NIR sub-device ensures low optical crosstalk below 1690 nm.

To evaluate the overall performance of the device, the total noise of the device is tested by a low-frequency noise spectrum analyzer under different biases. The noise analyzer collects data while the device is placed in a shield to reduce the interference of the stray light from the external environment. The theoretical value of the white noise power spectral density can be calculated by (2), where $k_B$ is the Boltzmann constant, *Re* is the differential resistance, *q* is the electron charge, and *I* is the dark current under bias.

$$I_n^2/\Delta f = 2qI + \frac{4K_BT}{Re} \qquad (2)$$

The total noise of the device under 0.1 V and −0.4 V are shown in Fig. 7. In low frequency region, the measured results exceed the theoretical calculation by several orders of magnitude, which is due to the presence of 1/*f* noise. In the high frequency flat regime, the measured white noise values agree with the calculated results. The inset of Fig. 7 shows the dependence of noise on bias voltages at 1 MHz, indicating that the noise level increases as the bias voltage increases, and that noise under negative bias (working at eSWIR band) is overall more significant than the noise under positive bias (working at NIR band).

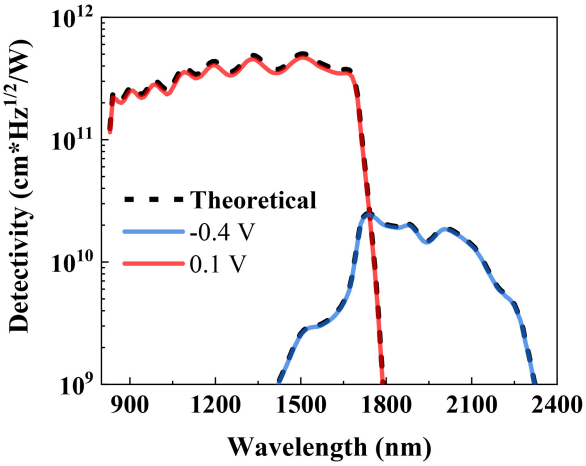


Fig. 8. Specific detectivity D∗ measured in front-side illumination for NIR sub-detector under 0.1 V and SWIR sub-detector under −0.4 V, respectively. The dashed line is calculated using the theoretical value of white noise, and the solid line is calculated by the mean of measured white noise.

Finally, the specific detectivity D∗ is calculated according to (3) [32], where *R* is the detector responsivity, *A* is the device area.

$$D^* = \frac{R\sqrt{A}}{\sqrt{I_n^2/\Delta f}} \qquad (3)$$

The detectivity of the device under 0.1 V and −0.4 V are shown in Fig. 8, where the dashed line is calculated using the theoretical value of noise while the solid line indicates D∗ is calculated by the mean value of measured noise in the high frequency flat regime. Under 0.1 V, the NIR sub-detector is turned on, and its peak D∗ reaches $4.69 \times 10^{11}$ cm· $Hz^{1/2}$/W at 1510 nm. And when the bias voltage turns to −0.4 V, the operation band of the detector switches to the eSWIR band, with the peak value reaching $2.43 \times 10^{10}$ cm· $Hz^{1/2}$/W, at 1740

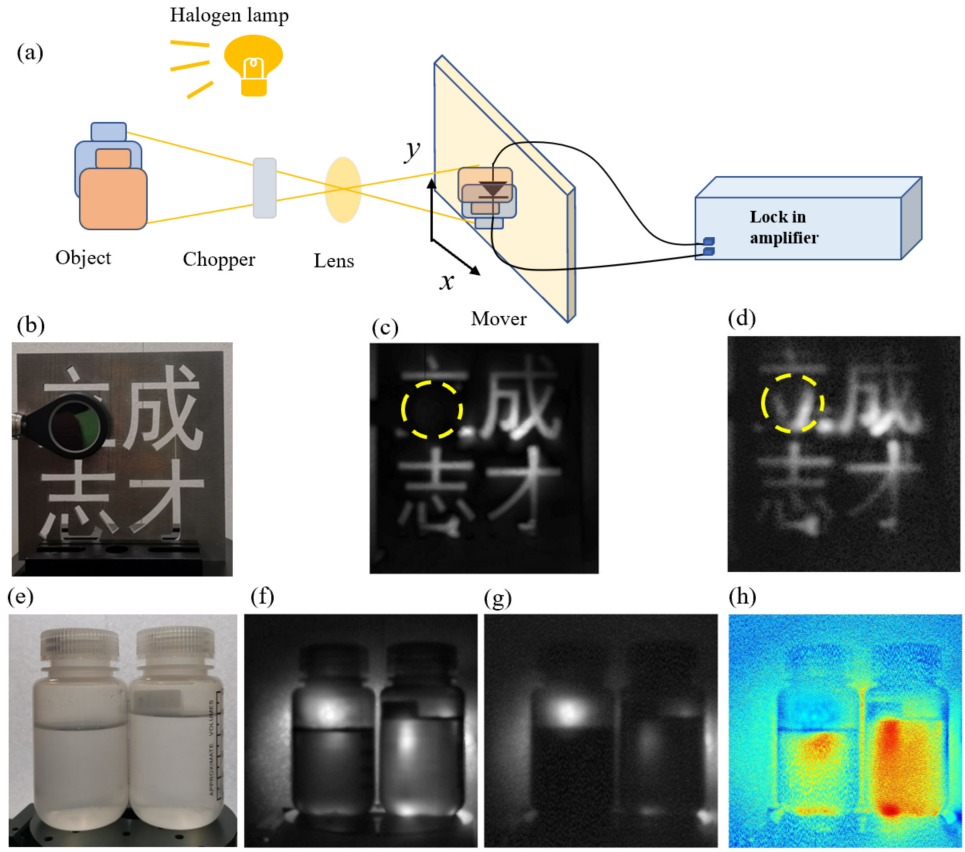


Fig. 9. (a) Schematic diagram of the single-pixel imaging system. Four Chinese characters are taken by (b) visible CMOS camera; (c) NIR InGaAs sub-detector (resolution: 400 × 400); (d) eSWIR T2SL sub-detector, the yellow dashed circle indicates the 1850 nm long-pass filter (resolution: 400 × 400). Water and acetone solution are taken by (e) visible CMOS camera; (f) the NIR sub-detector (resolution: 500 × 500); (g) the eSWIR InGaAs sub-detector (resolution: 500 × 500); (h) the calculated differential image.

nm. Compared with the NIR /eSWIR dual-band photodetectors reported previously [11], [13], [14], the D∗ of 1.85 × $10^{10}$ cm·$Hz^{1/2}$/W at 2 $\mu$m is nearly one order of magnitude larger.

## IV. Pixel Imaging

We also built a single-pixel imaging system to demonstrate the dual-band detection capability, as shown in Fig. 9(a). A broad-spectrum halogen lamp casts light on the object. Light transmitted or reflected by the object propagates through the lens and forms an image plane in which the detector moves. Then generated optical signal in the image plane is modulated by a 180 Hz chopper in the optical path and captured by a lock-in amplifier. The whole system is operating under room temperature.

In Fig. 9(b), there are four Chinese characters in which an 1850 nm long-pass filter blocks the first one. The information behind the filter is unreadable in visible CMOS camera (Fig. 9(b)) and NIR detector imaging (Fig. 9(c)) while could be captured by T2SL eSWIR sub-detector (Fig. 9(d)). Dual-band detection could supplement information unattainable from single-band detection.

In addition, we can also take advantage of the dual-band detection to distinguish between objects which are indistinguishable under single band detection. Two bottles of water and acetone solution are on the stage for imaging, as shown in Fig. 9(a). They are transparent in visible light (Fig. 9(e)) but have strong absorption with different absorption coefficients in the NIR and eSWIR band, respectively [33], [34]. We captured the NIR image (Fig. 9(f)) and eSWIR image (Fig. 9(g)) of the two bottles of the solution by switching the bias voltage of the detector. The NIR image is less noisy than the eSWIR image due to the higher D∗ and lower dark current of the NIR InGaAs sub-detector. And the differential image is calculated for better recognition of the two bottles of the solution according to (4) [13]. In (4), *C* is a parameter used to enhance or reduce the contrast of the picture, and in this work, *C* is chosen to be 0.15. The obtained differential image is shown in Fig. 9(h); the difference between the two bottles is noticeable.

$$IMG_{diff} = \frac{IMG_{0.1V} - IMG_{-0.4V}}{IMG_{0.1V} + IMG_{-0.4V} + C} \tag{4}$$

## V. Conclusion

In this study, we demonstrate a vertical stacked NIR/eSWIR dual-band detector based on InGaAs and $In_{0.53}Ga_{0.47}As$/$GaAs_{0.5}Sb_{0.5}$ T2SL. The AlAsSb barrier layer ensures the independent working of the two sub-detectors. At 0.1 V, the InGaAs sub-detector operates in the NIR band with a cutoff wavelength at 1750 nm. The dark current density of the detector at 300 K is

$7.35 \times 10^{-5}$ A/cm$^2$, and the peak responsivity reaches 0.88 A/W at 1510 nm, with a corresponding D$*$ of $4.69 \times 10^{11}$ cm·Hz$^{1/2}$/W. At $-0.4$ V, the T2SL eSWIR sub-detector covers 1700 nm to 2400 nm. The 300 K dark current density of is $8.68 \times 10^{-4}$ A/cm$^2$ and the responsivity at 2 $\mu$m is 0.21 A/W, with D$*$ up to $1.85 \times 10^{10}$ cm·Hz$^{1/2}$/W. In addition, a single-pixel imaging system is built to demonstrate the capability of dual-band detectors in information capturing and target recognition.

## ACKNOWLEDGMENT

The author would like to thank the device fabrication support from the ShanghaiTech University Quantum Device Lab.

## REFERENCES

[1] A. Rogalski, "Recent progress in infrared detector technologies," *Infrared Phys. Technol.*, vol. 54, no. 3, pp. 136–154, 2011.
[2] X. Tang, M. M. Ackerman, M. Chen, and P. Guyot-Sionnest, "Dual-band infrared imaging using stacked colloidal quantum dot photodiodes," *Nature Photon.*, vol. 13, no. 4, pp. 277–282, 2019.
[3] A. M. Hoang, A. Dehzangi, S. Adhikary, and M. Razeghi, "High performance bias-selectable three-color short-wave/mid-wave/long-wave infrared photodetectors based on type-II InAs/GaSb/AlSb superlattices," *Sci. Rep.*, vol. 6, Apr. 2016, Art. no. 24144.
[4] X. Wu, M. Kim, H. Qu, and Y. Wang, "Single-defect spectroscopy in the shortwave infrared," *Nature Commun.*, vol. 10, no. 1, Jun. 2019, Art. no. 2672.
[5] A. Gonzalez *et al.*, "Pedestrian detection at day/night time with visible and FIR cameras: A comparison," *Sensors*, vol. 16, no. 6, Jun. 2016, Art. no. 820.
[6] R. Sidhu, N. Duan, J. C. Campbell, and A. L. Holmes, "A long-wavelength photodiode on InP using lattice-matched GaInAs-GaAsSb type-II quantum wells," *IEEE Photon. Technol. Lett.*, vol. 17, no. 12, pp. 2715–2717, Dec. 2005.
[7] B. Chen and A. L. Holmes, "InP-based short-wave infrared and midwave infrared photodiodes using a novel type-II strain-compensated quantum well absorption region," *Opt. Lett.*, vol. 38, no. 15, pp. 2750–2753, 2013.
[8] A. Haddadi, R. Chevallier, G. Chen, A. M. Hoang, and M. Razeghi, "Bias-selectable dual-band mid-/long-wavelength infrared photodetectors based on InAs/InAs$_{1-x}$Sb$_x$ type-II superlattices," *Appl. Phys. Lett.*, vol. 106, no. 1, 2015, Art. no. 011104.
[9] A. M. Hoang, G. Chen, A. Haddadi, and M. Razeghi, "Demonstration of high performance bias-selectable dual-band short-/mid-wavelength infrared photodetectors based on type-II InAs/GaSb/AlSb superlattices," *Appl. Phys. Lett.*, vol. 102, no. 1, 2013, Art. no. 011108.
[10] V. M. More, Y. Kim, J. Jeon, J. C. Shin, and S. J. Lee, "Dual-band unipolar barrier infrared photodetector based on InGaAsSb bulk and type-II InAs/GaSb superlattice absorbers," *J. Alloys Compounds*, vol. 868, 2021, Art. no. 159195.
[11] Z. Xie, Z. Deng, X. Zou, and B. Chen, "InP-based near infrared/extended-short wave infrared dual-band photodetector," *IEEE Photon. Technol. Lett.*, vol. 32, no. 16, pp. 1003–1006, Aug. 2020.
[12] Z. Xie, Z. Deng, and B. Chen, "InP based SWIR dual-band photodetector," in *Proc 14th Pacific Rim Conf. Lasers Electro-Opt.*, 2020, Paper C11B_2.
[13] E. T. Simola *et al.*, "CMOS-Compatible bias-tunable dual-band detector based on GeSn/Ge/Si coupled photodiodes," *ACS Photon.*, vol. 8, no. 7, pp. 2166–2173, 2021.
[14] S. Park *et al.*, "Monolithic two-color short-wavelength InGaAs infrared photodetectors using InAsP metamorphic buffers," *Appl. Surf. Sci.*, vol. 581, 2022, Art. no. 152421.
[15] B. Chen, W. Jiang, J. Yuan, A. L. Holmes, and B. M. Onat, "SWIR/MWIR InP-Based p-i-n photodiodes with InGaAs/GaAsSb Type-II quantum wells," *IEEE J. Quantum Electron.*, vol. 47, no. 9, pp. 1244–1250, Sep. 2011.
[16] C.-H. Pan, C.-H. Chang, and C.-P. Lee, "Room temperature optically pumped 2.56-μm lasers with 'W' type InGaAs/GaAsSb quantum wells on InP substrates," *IEEE Photon. Technol. Lett.*, vol. 24, no. 13, pp. 1145–1147, Jul. 2012.
[17] B. Chen, W. Y. Jiang, and A. L. Holmes, "Design of strain compensated InGaAs/GaAsSb type-II quantum well structures for mid-infrared photodiodes," *Opt. Quantum Electron.*, vol. 44, no. 3, pp. 103–109, Jun. 2012.
[18] B. Chen, A. Holmes, V. Khalfin, I. Kudryashov, and B. M. Onat, "Modeling of the type-II InGaAs/GaAsSb quantum well designs for mid-infrared laser diodes by kp method," in *Proc. Laser Technol. for Defense Secur. VIII*, 2012, vol. 8381, Art. no. 83810F.
[19] B. Chen and L. H. Archie Jr, "Carrier dynamics in InP-based PIN photodiodes with InGaAs/GaAsSb type-II quantum wells," *J. Phys. D: Appl. Phys.*, vol. 46, no. 31, 2013, Art. no. 315103.
[20] B. Chen, J. Yuan, and A. L. Holmes, "Dark current modeling of InP based SWIR and MWIR InGaAs/GaAsSb type-II MQW photodiodes," *Opt. Quantum Electron.*, vol. 45, no. 3, pp. 271–277, Mar. 2013.
[21] T. Kawahara *et al.*, "InGaAs/GaAsSb type-II quantum-well focal plane array with cutoff-wavelength of 2.5 $\mu$m," in *Proc. Quantum Sens. Nano Electron. Photon. XIV*, 2017, vol. 10111, Art. no. 1011115.
[22] Y. Chen *et al.*, "Dynamic model and bandwidth characterization of InGaAs/GaAsSb type-II quantum wells PIN photodiodes," *Opt. Exp.*, vol. 26, no. 26, pp. 35034–35045, 2018.
[23] Y. Chen, Z. Zhou, P. Ma, and B. Chen, "Nonlinear characteristics of uni-traveling carrier photodiode with InGaAs/GaAsSb type-II multiple quantum wells absorber," *J. Lightw. Technol.*, vol. 38, no. 17, pp. 4867–4873, 2020.
[24] Y. Chen, Z. Xie, J. Huang, Z. Deng, and B. Chen, "High-speed uni-traveling carrier photodiode for 2 $\mu$m wavelength application," *Optica*, vol. 6, no. 7, pp. 884–889, 2019.
[25] Hamamatsu, "Two-color detector K12729-010K." Accessed: 2020. [Online]. Available: https://www.hamamatsu.com/jp/en/product/type/K12729-010K/index.html
[26] J. Huang, Z. Xie, Y. Chen, J. E. Bowers, and B. Chen, "High speed mid-wave infrared uni-traveling carrier photodetector," *IEEE J. Quantum Electron.*, vol. 56, no. 4, Aug. 2020, Art. no. 4000807.
[27] B. F. Andresen *et al.*, "SU-8 passivation of type-II InAs/GaSb strained layer superlattice detectors," in *Proc. Infrared Technol. Appl. XXXVI*, 2010, vol. 7660, Art. no. 76601U.
[28] D. Cohen-Elias, Y. Uliel, N. Cohen, I. Shafir, O. Westreich, and M. Katz, "Short wavelength infrared pBn GaSb/AlAsSb/InPSb photodetector," *Infrared Phys. Technol.*, vol. 85, pp. 81–85, 2017.
[29] J. Lu *et al.*, "Effect of SU-8 passivation layer induced stress on the performance of GaSb diode," *IEEE Photon. Technol. Lett.*, vol. 30, no. 11, pp. 1060–1063, Jun. 2018.
[30] E. Plis, N. Gautam, S. Myers, Y. Sharma, L. R. Dawson, and S. Krishna, "Reduction of surface leakage current in InAs/GaSb strained layer long wavelength superlattice detectors using SU-8 passivation," *Appl. Phys. Lett.*, vol. 97, no. 14, 2010, Art. no. 143512.
[31] K. Swaminathan, T. J. Grassman, L. M. Yang, Q. Gu, M. J. Mills, and S. A. Ringel, "Optically-aligned visible/near-infrared dual-band photodetector materials and devices on GaAs using metamorphic epitaxy," *J. Appl. Phys.*, vol. 110, no. 6, 2011, Art. no. 063109.
[32] Z. Xie, Z. Deng, J. Huang, Z. Xie, Z. Zhou, and B. Chen, "InP-based extended-short wave infrared heterojunction phototransistor," *J. Lightw. Technol.*, vol. 39, no. 14, pp. 4814–4819, 2021.
[33] J. J. Max and C. Chapados, "Infrared spectroscopy of acetone-water liquid mixtures. II. Molecular model," *J. Chem. Phys.*, vol. 120, no. 14, pp. 6625–6641, Apr. 2004.
[34] Brisort, "Spectroscopy." Accessed: 2020. [Online]. Available: http://www.brisort.com/zh/product_cg349231.html